

## Article

# Observation of Pattern Formation during Electromagnetic Levitation Using High-Speed Thermography

Yindong Fang <sup>1</sup>, Dongmei Liu <sup>1</sup>, Yongfu Zhu <sup>2</sup>, Peter K. Galenko <sup>1,3</sup> and Stephanie Lippmann <sup>1,\*</sup><sup>1</sup> Otto Schott Institute of Materials Research, Friedrich Schiller University Jena, 07743 Jena, Germany<sup>2</sup> Key Laboratory of Automobile Materials of Ministry of Education, Jilin University, RenMin Street 5988, Changchun 130022, China<sup>3</sup> Laboratory of Multi-Scale Mathematical Modeling, Department of Theoretical and Mathematical Physics, Ural Federal University, Lenin Ave. 51, Ekaterinburg 620000, Russia

\* Correspondence: stephanie.lippmann@uni-jena.de

**Abstract:** Electromagnetic levitation (EML) was employed for studying the velocity and morphology of the solidification front as a function of undercooling of metallic materials. The limitation of the EML technique with respect to low melting alloys that emit outside the visible light spectrum was overcome by employing state-of-the-art high-speed mid-wavelength infrared cameras (MWIR cameras) with a photon detector. Due to the additional thermography contrast provided by the emission contrast of the solid and liquid phases, conductor, and semi-conductor, the pattern formation of Al-based alloys was studied in detail, revealing information on the nucleation, phase selection during solidification, and the influence of convection.

**Keywords:** electromagnetic levitation; phase transformation; in-situ observation; phase selection



**Citation:** Fang, Y.; Liu, D.; Zhu, Y.; Galenko, P.K.; Lippmann, S. Observation of Pattern Formation during Electromagnetic Levitation Using High-Speed Thermography. *Crystals* **2022**, *12*, 1691. <https://doi.org/10.3390/cryst12121691>

Academic Editor: George Kenanakis

Received: 23 October 2022

Accepted: 16 November 2022

Published: 22 November 2022

**Publisher's Note:** MDPI stays neutral with regard to jurisdictional claims in published maps and institutional affiliations.



**Copyright:** © 2022 by the authors. Licensee MDPI, Basel, Switzerland. This article is an open access article distributed under the terms and conditions of the Creative Commons Attribution (CC BY) license (<https://creativecommons.org/licenses/by/4.0/>).

## 1. Introduction

The Use of electromagnetic levitation (EML) facilities is a well-established method for directly monitoring the solidification process of conductive samples and evaluating various thermophysical parameters of the liquid phase using pyrometers and high-speed cameras [1]. To obtain substantial undercoolings (typical up to 20% of the melting temperature), samples are freely levitated in an ultraclean environment throughout the experiment, thereby avoiding or minimizing heterogeneous nucleation sites at the crucible wall or impurities, respectively [2,3]. The process allows for the fabrication of materials with metastable phase equilibria that possess new physical properties, such as quasicrystals, metallic glasses, supersaturated solids, and grain-refined materials [4–6].

Previous studies report various in-situ observation methods that are combined with EML setups. The first published method by Schleip et al. in 1988 used two silicon photodiodes with a response time of 1  $\mu$ s to catch the recalescence front and measure the growth velocity of dendrites [7,8]. A metal needle was positioned at the south pole of the sample and triggered solidification. The photodiodes recorded the recalescence generated by the liquid–solid phase transition, and the solidification length and time interval between two heating signals were utilized to calculate the dendritic growth velocity. Later, Eckler et al. provided an idea to measure the solidification time from the sample bottom to top by using capacitance proximity sensors (CPS) [9,10], a technique with a measurement principle similar to the photodiode technique. The microstructure of the levitated samples was studied post-mortem after complete solidification (see Figures 1 and 2). The reliability of the above-mentioned photodiode-related methods relies on the relative spatial position of the solidification direction and recalescence front. In this arrangement, in the worst-case scenario, the photodiode misses the event of recalescence. In addition, the applied external trigger, which is also used to control the solidification direction, can stick to the sample

and lead to a contamination of the sample during the solidification process, hindering the analysis.

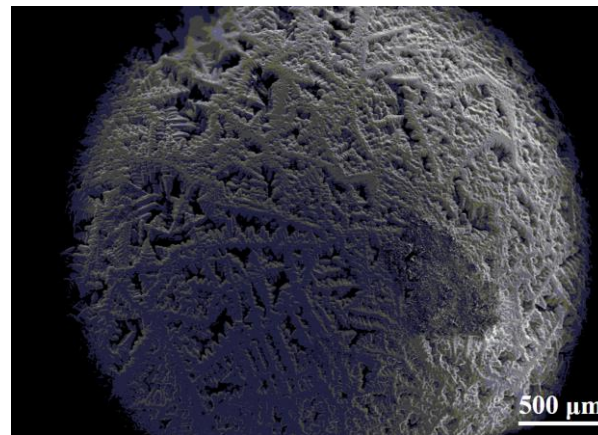


**Figure 1.** Outer surface of a droplet processed in an EML facility.

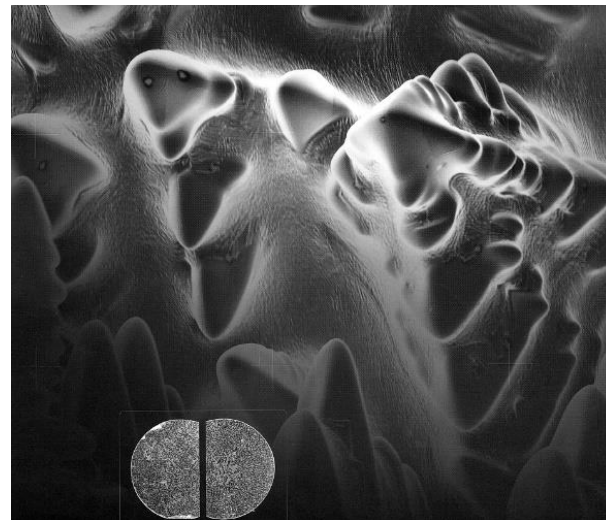


**Figure 2.** Dendritic structure of an EML droplet.

With the development of image-recording technology, the use of high-speed cameras (HSC) has allowed for the more detailed study of microstructure formation during EML experiments [11,12]. It permits in-situ recording of half of the sample surface with enhanced spatial resolution and enables the visualization of the path of recalescence fronts across the entire surface of the droplet during periods of milliseconds or less. Matson was the first to describe the recalescence front morphology and crystallization kinetics for the solidification of nickel droplets using HSC (see Figure 3) [11]. In this case, the requirement for an external trigger for nucleation is eliminated. When compared with both the CPS approach and the photodiode technique, the effectiveness of the measurements is exceptionally high. Not only was it feasible to capture the progression of the recalescence fronts at various levels of undercooling, but it also provided proof of the formation of metastable phases [13]. Hartmann et al. found, in 2008, the formation of a metastable phase with a transition to a stable phase in the form of a double recalescence in titanium–aluminum alloys (see Figure 4). In both cases, as presented in Figures 3 and 4, one can well observe and evaluate recalescence fronts; however, they cannot be linked directly to the crystalline structure of the bulk. With the use of mathematical methods of simulation, it became possible to visualize both the two-dimensional structure of the recalescence/crystallization front and the internal crystalline structure of the solidifying droplet (see Figure 5) [14].

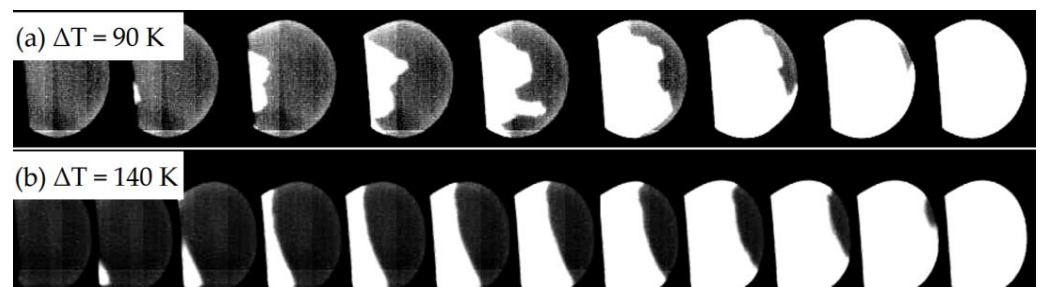


**Figure 3.** Visualization of the solidification front as it propagates through the nickel sample [11]: solidification was triggered for initial undercooling (a)  $\Delta T = 90$  K and (b)  $\Delta T = 140$  K. Copyright 1998 The Minerals, Metals & Materials Society; used with permission.

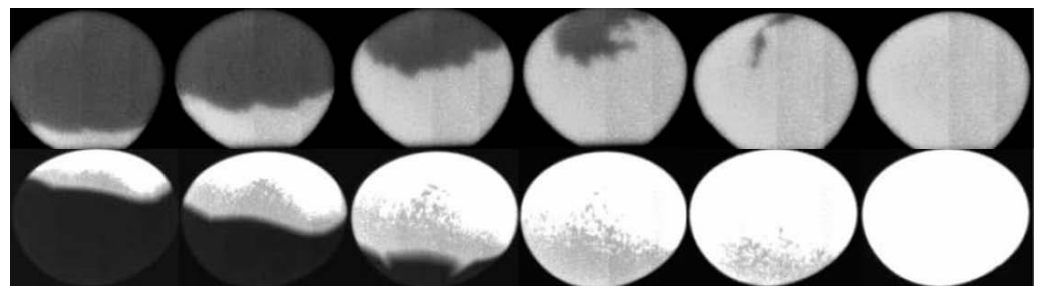


**Figure 4.** Evolution of recalescence fronts over the surface of droplets from the  $\text{Ti}_{45}\text{Al}_{55}$  alloy for different initial undercoolings [13]. The upper time sequence of droplet solidification shows the structure of the recalescence front after reaching the initial supercooling  $\Delta T = 120$  K. In this case, a stable face-centered cubic lattice (FCC-lattice) of the  $\gamma$ -phase is formed. The lower time sequence of droplet solidification shows the structure of the recalescence front after reaching the initial undercooling  $\Delta T = 286$  K with the formation of a metastable hexagonal close-packed lattice (HCP-lattice) first and then a stable FCC-lattice of the  $\gamma$ -phase. Copyright 2008 Elsevier Publishing; used with permission.

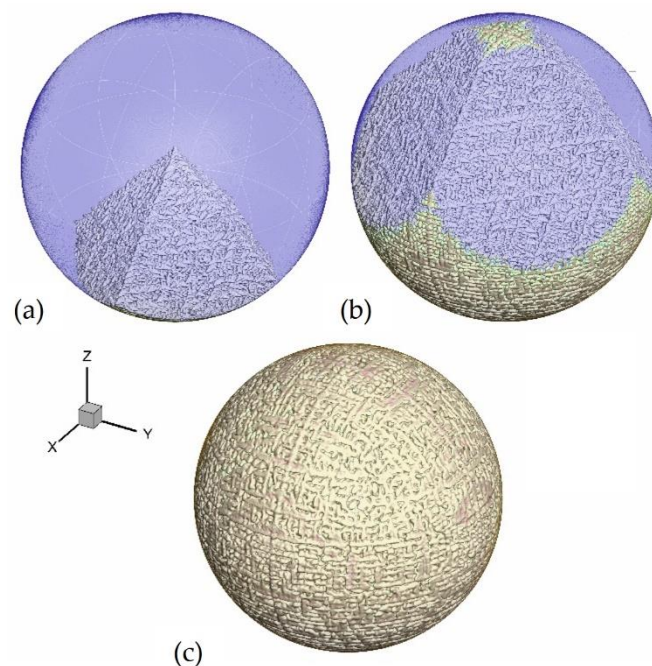


**Figure 5.** Simulated evolution of the dendritic structure of a glass-fluxed sample of pure nickel at different stages of solidification [14]. (a) Early stage of recalescence. (b) Late stage of recalescence. (c) Coarsening process.

The time resolution of the HSC technique is several orders lower than that of the CPS technique, which is a drawback of the HSC method. In addition, high-speed cameras operating in the visible light spectrum only allow for an observation temperature starting from 798 K (Draper point) [15]. In contrast, IR and MWIR Bolometer cameras operate at lower temperatures but lack the necessary frame rate to capture the solidification process. For those reasons, the in-situ observation of low-melting alloys with EML was impossible until the present [16]. Now, state-of-the-art MWIR photon-detector cameras that use the photo effect instead of the change in resistivity, as with bolometer cameras, offer significantly higher rates of data acquisition: 30,000 fps instead of the 60 fps for bolometer cameras [17]. Although, they do not match the acquisition rate of VIS high-speed cameras, they offer, for the first time, the possibility to investigate the melting and solidification process in low-melting alloys [18,19].

In addition to optical high-speed cameras, X-ray diffractometry is also employed for visualizing surface patterns. It is possible to indirectly reproduce primary or secondary pattern formation during droplet solidification. As an example, using time-resolved two-dimensional X-ray diffractometry, K. Nagashio et al. investigated the spontaneous dendrite fragmentation during solidification from undercooled Si melt and found that the fragmentation occurred after recalescence at the initial stage of the “temperature-time” plateau period [20]. Such an analysis allows us to verify and correct the existing theories on crystal’s growth and fragmentation models. Time-resolved in-situ high-energy X-ray diffraction also provides the opportunity to study the liquid–liquid and liquid–solid transformation, the phase selection, and phase fractions in real time in containerless rapid solidification processes [21].

This article explored the possibility of implementing high-speed MWIR cameras in EML facilities for studying the solidification process of low-melting alloys, such as Al-rich binary alloys with melting points below 923 K. Details such as the phase selections at various undercoolings and local conditions were analyzed in-situ by employing a state-of-the-art photon detector camera in combination with post-mortem microstructure analysis.

## 2. Experiment

The alloys used in this study were Al–30.6 wt.% Cu, Al–6 wt.% Ni, Al–16 wt.% Si, and Al–20 wt.% Si, which were prepared by melting 4 N purity aluminum, copper, nickel, or silicon, respectively, in an inductive furnace with a cold wall crucible; for details, see ref. [19]. After verifying the nominal composition with Energy Dispersive X-Ray Analysis (EDX analysis), the samples were cut and ground to 500 mg cubes and then stored in isopropyl to prevent pollution and oxidation.

A schematic view of the EML facility is sketched in Figure 6. In general, the design of the levitation system consists of

- a gas pumping system to reach the vacuum within the levitation camera deep enough to prevent the oxidation of the sample surface as much as possible;
- a conical or cylindrical coil, inside which the alternating electric current produces the electromagnetic field directed in the side opposite to the direction of the gravitational field;
- a droplet which may levitate if the balance between electromagnetic and gravitational fields is reached within the coil and strong enough to pick up the droplet from the initial holder;
- a pump or gas ejector to let in cooling gas (hydrogen-helium mixture or argon) to cool down the melted droplet (after its heating due to electric current flowing in the droplet from the induced alternating electromagnetic field);
- a triggering needle to initiate the process of crystallization (the needle should be made from the same material/alloy as the droplet itself).

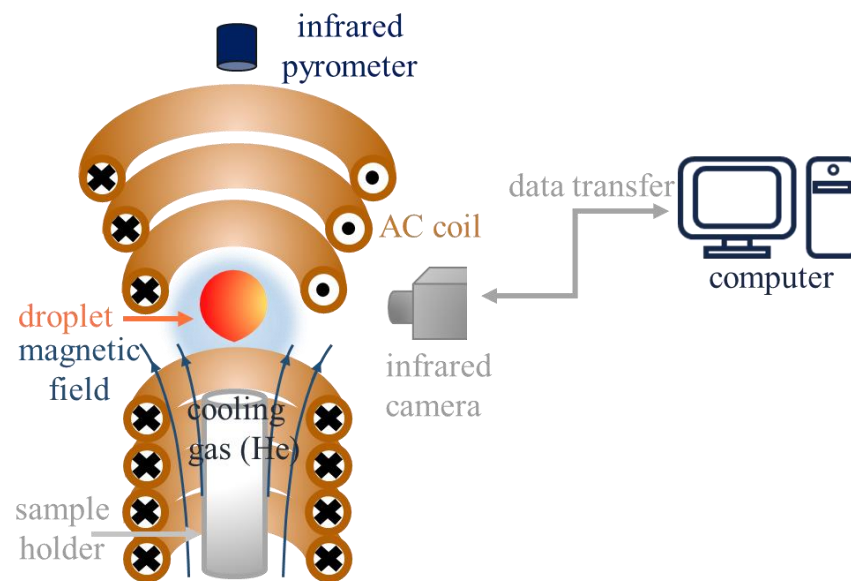


**Figure 6.** Schematic of the electromagnetic levitation (EML) facility with a high-speed MWIR camera for recording the solidification process of low-melting alloys.

The levitation process is controlled by the power of the high-frequency generator, which supplies current to the coil to create an electromagnetic field with the power necessary to levitate a specific sample of a given mass and geometry. In the present work, the square samples had a side length of 5 to 7 mm and were placed on a sample holder between the upper and lower coil. An alternating current with a frequency of  $f \approx 300$  kHz and a power of  $P = 0.3$  to 10 kW was applied for generating an electromagnetic field. The coil design was optimized in order to counteract gravity and heat the sample [22]. For each sample, several heating and cooling cycles were applied, and the solidification process was monitored by pyrometer and a high-speed MWIR camera. The infrared camera utilized in this study was an IR-8300 manufactured by InfraTec GmbH, Germany, with an area detector of  $640 \times 480$  pixels (max. resolution  $15 \mu\text{m} \times 15 \mu\text{m}$  per pixel) and a temperature range from  $-40$  to  $1500$  °C. The camera was situated outside the vacuum chamber, and an MWIR transparent calcium fluoride window was used for observation. The images were captured at a frame rate of 670 fps with a size of  $320 \times 240$  pixels<sup>2</sup>. For data acquisition (samples size, temperature distribution), the software IRBIS<sup>®</sup>3 by InfraTec GmbH, Germany was used. The temperature-time profiles were continuously measured by an infrared pyrometer on the top of the sample. A high-purity He (6 N) gas flow was applied for additional cooling. After the last cycle, the surfaces of all the samples were directly observed by scanning electron microscopy (SEM). Then, the samples were cut from the middle, embedded, and polished to  $1 \mu\text{m}$  for detailed microstructural analysis.

### 3. Results

#### 3.1. In-Situ Observation of Pattern Formation and Micrographs of Al–30.6 wt.% Cu Alloy

A sequence of thermograms recorded during the solidification process of Al–30.6 wt.% Cu is shown in Figure 7. The thermograms at 0 s and 0.012 s show the growth of a dendritic solid–liquid (S/L) front. The distinction between oxide and metallic phases was made by emissivity. Measured front positions and estimated growth velocities are frequently used for determining simulation parameters and serve as the model refinement for dendritic growth at higher undercoolings [23]. In the thermograms from 1.407 s to 1.493 s, the subsequent formation of eutectic cells was visible. Several eutectic cells grew simultaneously and formed eutectic grains. The resulting fine structures are shown in the micrograph of the cross-section in Figure 8. There existed features of the primary phase, which can be described as fragmented dendrites. The fragmentation is caused by local remelting initiated by the release of latent heat during the solidification of eutectic or due to

convection. The lamellar spacing of eutectic was not uniform. When following the enlarged eutectic pattern, a “honeycomb” structure became visible with fine eutectic in the grain interior. The “honeycomb” structure has been reported in the literature before [24,25], but the formation has thus far been subject to speculation.

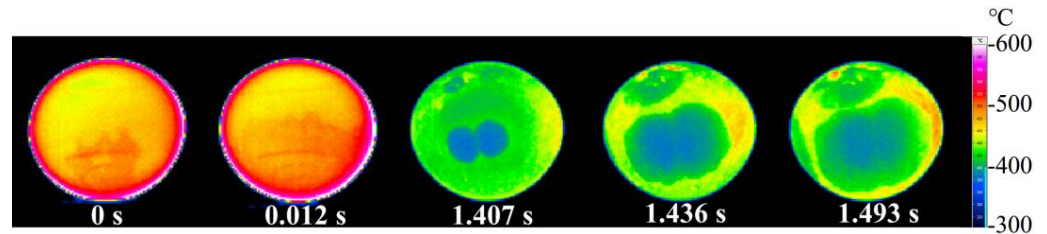


**Figure 7.** Image sequence of the solidification process of Al–30.6 wt.% Cu showing the formation of primary dendrites and eutectic cells. The droplet was solidified from the initial undercooling  $\Delta T = 40$  K.

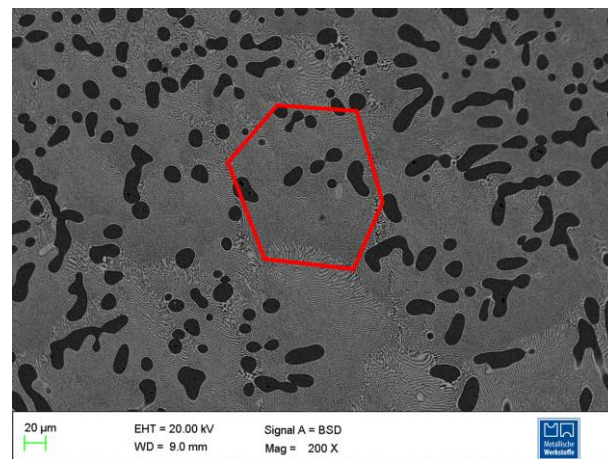


**Figure 8.** Honeycomb structure in Al–30.6 wt.% Cu with coarse cell walls and fine-grain interior after the EML experiment. Red hexagon shows the typical honeycomb structure.

### 3.2. In-Situ Observation of Pattern Formation and Micrographs of Al–6 wt.% Ni Alloy

The solidification process of Al–6 wt.% Ni is given in Figure 9. The primary  $\alpha$ -Al phase formed and grew, and the motion of the S/L interface was traceable from the upper right to the lower left (0–0.151 s). From  $t = 0.172$ , a spiral cluster developed ahead of the solidification front, interacting with the primary phase coming from different directions.

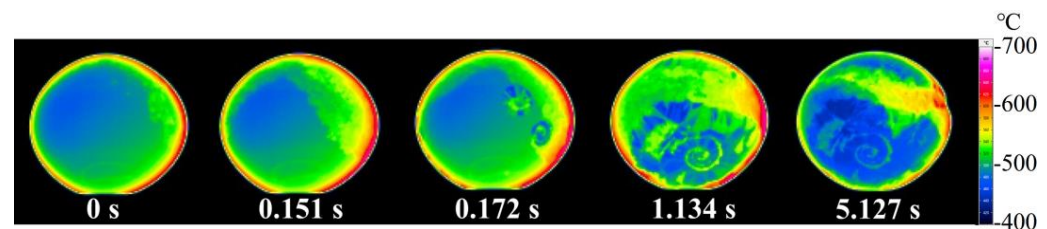


**Figure 9.** Image sequence of the solidification process of Al–6 wt.% Ni alloy showing the formation of a spiral cluster ahead of the solidification front. The droplet was solidified from the initial undercooling  $\Delta T = 47$  K.

The spiral cluster is marked with a white square in the micrograph (contrast given by Back-Scatter Electron (BSE) diffraction) in Figure 10a. The micrograph complements the observations; the spiral in the thermogram is composed of eutectic (light grey in BSE, green in thermogram) and an  $\alpha$ -Al phase (dark grey in BSE, blue in thermogram). The formation

of the spiral is related to convection that transports hot melt and solute to the dendritic solidification front, leading to a partial remelting of  $\alpha$ -Al primary dendrites. The release of latent heat during the formation of eutectic is another heat source that may cause the remelting of the primary dendrites, see Figure 10b,c. The eutectic was rod-like (or fibrous) and was found between the partially melted  $\alpha$ -Al phases dendrites, as shown in Figure 10d.

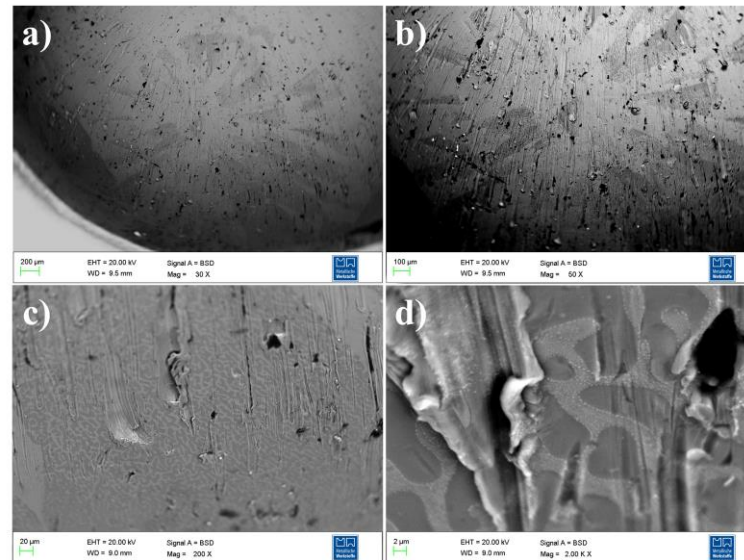


**Figure 10.** Micrograph of spiral cluster shown in thermogram  $t = 1.134$  s (Figure 9) in BSE contrast, details of partially melted  $\alpha$ -Al phase dendrites and rod-like eutectic revealing the disturbance of the solidification front and the local remelting of primary dendrites given at different magnifications (a–d).

### 3.3. In-Situ Observation of Pattern Formation and Micrographs of Al-16 wt.% Si Alloy

The thermograms in Figure 11 show the solidification sequence of Al-16 wt.% Si. Si nucleated first and acted as a nucleation site for eutectic growth (0 s), then eutectic cells grew in a circular pattern. At 0.727 s, a red layer formed around each individual cell. The comparison with the micrograph revealed it to be Si, which as a semiconductor has a significantly different emissivity. When the Si layer ceased to grow, the eutectic resumed forming until the solidification process was completed.

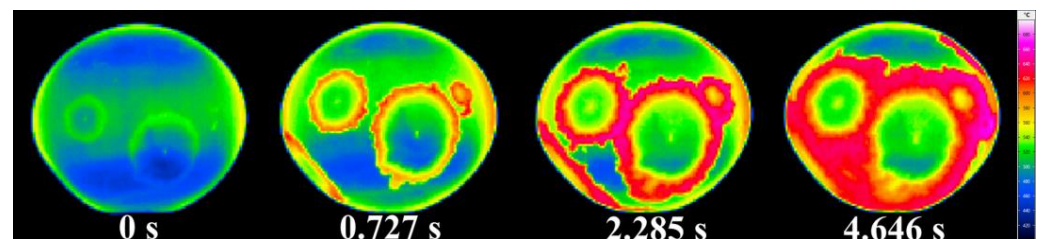


**Figure 11.** Solidification sequence of Al-16 wt.% Si alloy: primary Si, eutectic, Si layer, and followed by eutectic once more. The droplet was solidified from the initial undercooling  $\Delta T = 134$  K.

The primary Si at the surface of the Al-16 wt.% Si was also found by electron microscopy (see Figure 12). The eutectic cell that grew from the primary Si was also visible and validated by EDX. The micrograph of a cross-section in Figure 13 confirms the nucleation sequence observed by thermography: a fine eutectic surrounded the primary Si, then the solidification sequence changed to Si again and ended with the formation of a significantly coarser eutectic region.

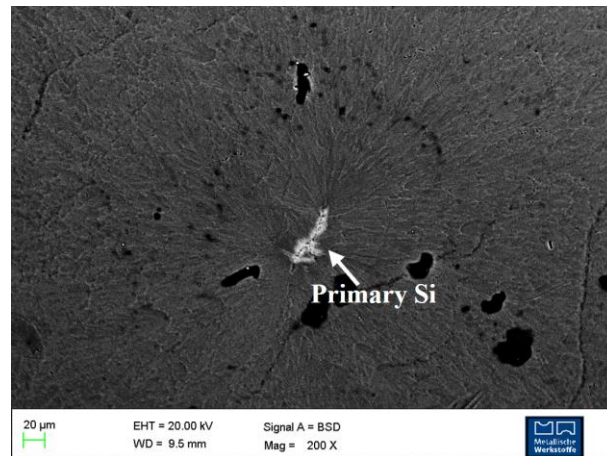


**Figure 12.** Micrograph of Al-16 wt.% Si showing primary Si in BSE contrast. EDX point scan shows the concentration of primary Si.

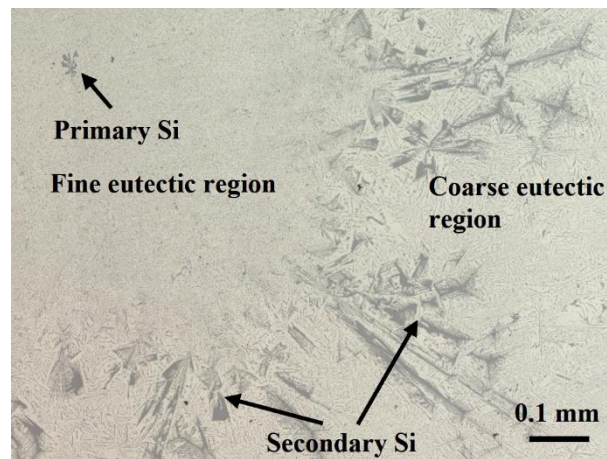


**Figure 13.** Optical microscope image of the cross-section of Al-16 wt.% Si confirming the solidification sequence observed by thermography: primary Si, subsequently grown fine eutectic, followed by Si once again, and coarse eutectic.

#### 3.4. In-Situ Observation of Pattern Formation and Micrographs of Al-20 wt.% Si Alloy

Al-20 wt.% Si alloy showed a completely different growth pattern in comparison with Al-16 wt.% Si (compare Figures 11 and 14). Primary Si nucleated at the helium-cooled side and grew upwards in the form of dendrites (see Figure 14). At 5.072 s, eutectic undercooling was reached and eutectic formed between the primary Si dendrites. The micrograph in Figure 15 shows an example for a well-developed primary Si dendrite on the sample surface.

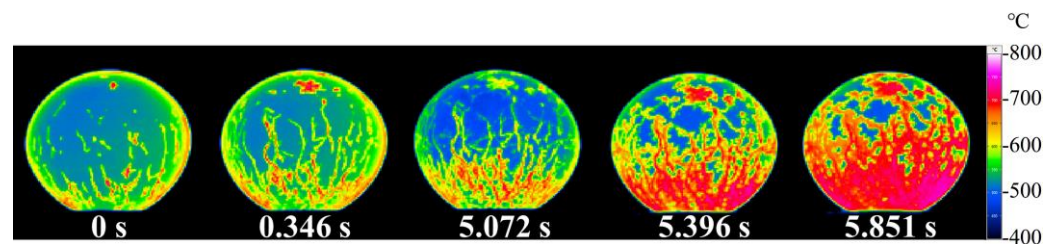


**Figure 14.** Thermograms of the solidification process of Al-20 wt.% Si at different times. The droplet was solidified from the initial undercooling  $\Delta T = 138$  K.

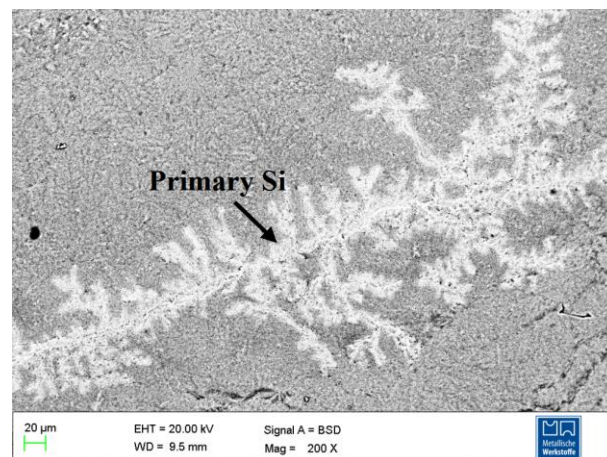


**Figure 15.** Micrograph (SEM image, BSE contrast) of Al-20 wt.% Si with well-developed primary Si dendrite surrounded by fine eutectic. The concentration of primary dendrite stem is obtained using an EDX point scan.

#### 4. Discussion

The combination of thermograms recorded in-situ with a high-speed MWIR camera during EML experiments and micrographs provides the possibility to study solidification in low-melting alloys at high undercoolings. The maximum frequency of 670 fps for  $320 \times 240$  pixel<sup>2</sup>, each pixel  $15 \times 15$  µm<sup>2</sup> allows the analysis of solid–liquid interface velocities up to 10 m/s.

In principle, it is also possible to measure local temperatures, but this requires calibration, taking the different emissivity of the melt and solid (incl. phase-specific emissions) and the curvature of the sample surface into account. This is so complex and subject to errors that the measurement of the sample temperature with a two-color pyrometer and the assignment of slope changes in the T-t diagrams to reactions is much more reliable.

For investigating the solidification process in-situ, however, the phase-specific emissivity provides the necessary contrast for the distinction of phases. By that, details of the solidification process, such as the formation of the honeycomb structure in Al-30.6 wt.% Cu, become comprehensible. Eutectic growth started at different positions simultaneously, and with increasing time the eutectic clusters grew closer to each other, the growth velocity decreased, and the eutectic became coarser.

For Al-6 wt.% Ni, the effects caused by strong convection became directly visible. During EML, convection is hard to avoid; it is induced by the strong alternating electric field [26] and by forced cooling with helium, the latter also causing temperature gradients from top to bottom. The remelting of the primary dendrites in Figure 10b may be caused by either latent heat released during the eutectic reaction in the interdendritic spacing or by convection that transports hot melt and solute. Since the remelting is more pronounced on the left side of the dendrites, convection is the most plausible explanation.

An alternating phase sequence was observed in Al-16 wt.% Si. A Si particle, as shown in Figure 11, was present in each center of the eutectic cells. The particle was either undissolved Si or formed at high undercoolings. The idea of undissolved Si is less likely since the samples were levitated in the liquid state for 3 min, 200 K above liquidus temperature before quenching. More likely, Si formed during cooling in the metastable temperature range. For the Au-Si system, another fcc-Si system, the formation of metastable phases was reported by Kurtuldu and Löffler [27]. Stable or metastable, when a Si-rich or pure Si particle forms from the melt at high undercoolings, its direct vicinity becomes depleted in Si and is heated by latent heat. In the present case, that seems to initiate coupled growth. The coupled zone in the Al-Si phase diagram in Figure 16 is highly asymmetric [28]. It is situated on the Si-rich side, i.e., the liquid in front of the eutectic will

be enriched in Si during the solidification of eutectic. When the supersaturation is high enough, Si nucleates a second time in front of the eutectic front as observed experimentally.

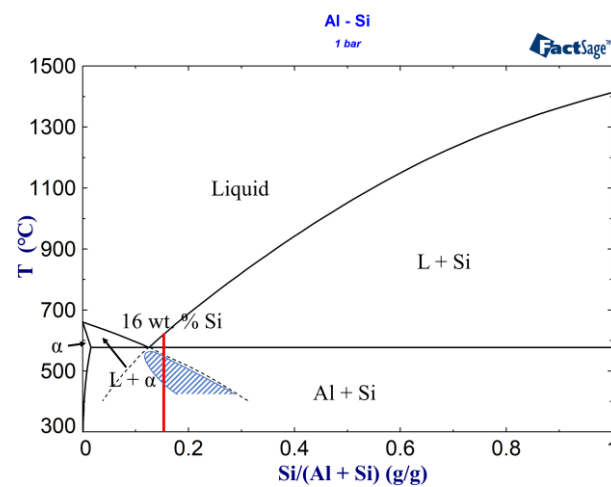


**Figure 16.** Al–Si phase diagram with unsymmetric coupled zone (blue dashed area).

In Al–20 wt.% Si, Si is the primary phase. The thermograms show the growth of Si dendrites from the bottom to the top of the sample, following the temperature gradient dictated by the He flow. At the top of the sample, Si dendrites grew without the influence of the temperature gradient. They showed a five-fold symmetry, typically observed in hypereutectic Al–Si alloys experiencing slow solidification rates [29]. The eutectic growth in between the Si dendrites started later, i.e., at higher undercoolings. In comparison with Al–16 wt.% Si, the macroscopic temperature gradient impeded the observation of alternating phases due to locally changing undercooling.

Even though high-speed VIS cameras have advantages that cannot be replaced by high-speed IR cameras in terms of resolution and shooting frame rate yet, high-speed IR cameras that operate in the middle wavelengths range fill the gap in low-melting alloys and allow the observation of solid–liquid phase transition in unprecedented detail.

## 5. Conclusions

This article demonstrated the possibility of studying the solidification processes of low-melting alloys during electromagnetic levitation experiments in unprecedented detail by employing a high-speed MWIR camera and high-precision optics. Contrast was reached via differences in the emissivity of the conductor and semiconductor, liquid and solid, as well as composition. Phase identification still requires a comparative analysis of the thermograms with micrographs or diffractograms.

**Author Contributions:** Y.F., Y.Z., P.K.G. and S.L. formal analysis. Y.F., D.L. and Y.Z. investigation. Y.F. data curation. P.K.G. and S.L. methodology. The authors contributed equally to the present re-search article. All authors have read and agreed to the published version of the manuscript.

**Funding:** The authors gratefully acknowledge financial support from DFG (LI 2827/2-1, RE 1261/23-2 and GA 1142/11-1); European Space Agency (ESA) within the project NEQUISOL under contract No. 15236/02/NL/SH, and Russian Science Foundation under project No. 21-19-00279.

**Institutional Review Board Statement:** Not applicable.

**Data Availability Statement:** Data are available by request to the corresponding author.

**Acknowledgments:** The authors specially thank the late Markus Rettenmayr for continuous support and fruitful discussions in all the year.

**Conflicts of Interest:** The authors declare no conflict of interest.

## References

1. Herlach, D.M. Containerless Undercooling and Solidification of Pure Metals. *Annu. Rev. Mater. Sci.* **1991**, *21*, 23–44. [[CrossRef](#)]
2. Sayavur, I.; Bakhtiyarov, D.A.S. Electromagnetic Levitation Part I: Theoretical and Experimental Considerations. *Fluid Dyn. Mater. Process.* **2008**, *4*, 99–112. [[CrossRef](#)]
3. Sayavur, I.; Bakhtiyarov, D.A.S. Electromagnetic Levitation Part II: Thermophysical Property Measurements in Terrestrial Conditions. *Fluid Dyn. Mater. Process.* **2008**, *4*, 163–184. [[CrossRef](#)]
4. Jones, H. *Rapid Solidification of Metals and Alloys*; The Institution of Metallurgists: London, UK, 1982.
5. Herlach, D.M.; Galenko, P.K.; Holland-Moritz, D. Metastable solids from undercooled melts. In *Pergamon Materials Series*; Elsevier: Amsterdam, The Netherlands, 2007.
6. Sayavur, I.; Bakhtiyarov, D.A.S. Electromagnetic Levitation Part III: Thermophysical Property Measurements in Microgravity. *Fluid Dyn. Mater. Process.* **2009**, *5*, 1–22. [[CrossRef](#)]
7. Schleip, E.; Willnecker, R.; Herlach, D.M.; Görlner, G.P. Measurements of ultrarapid solidification rates in greatly undercooled bulk melts with a high speed photosensing device. *Mater. Sci. Eng.* **1988**, *98*, 39–42. [[CrossRef](#)]
8. Willnecker, R.; Herlach, D.M.; Feuerbacher, B. Evidence of nonequilibrium processes in rapid solidification of undercooled metals. *Phys. Rev. Lett.* **1989**, *62*, 2707–2710. [[CrossRef](#)] [[PubMed](#)]
9. Eckler, K.; Kratz, M.; Egry, I. New technique of measuring dendrite growth velocities in undercooled metallic melts. *Rev. Sci. Instrum.* **1993**, *64*, 2639–2642. [[CrossRef](#)]
10. Eckler, K.; Herlach, D.M. Measurements of dendrite growth velocities in undercooled pure Ni-melts—Some new results. *Mater. Sci. Eng. A* **1994**, *178*, 159–162. [[CrossRef](#)]
11. Matson, D.M. The measurement of dendrite tip propagation velocity during growth into undercooled metallic melts. In *Solidification*; Chun, J.H., Marsh, S.P., Dantzig, J.A., Trivedi, R., Hofmeister, W., Chu, M.G., Lavernia, E.J., Eds.; TMS: Warrendale, PA, USA, 1998; pp. 233–241.
12. Funke, O.; Phanikumar, G.; Galenko, P.K.; Chernova, L.; Reutzel, S.; Kolbe, M.; Herlach, D.M. Dendrite growth velocity in levitated undercooled nickel melts. *J. Cryst. Growth* **2006**, *297*, 211–222. [[CrossRef](#)]
13. Hartmann, H.; Galenko, P.K.; Holland-Moritz, D.; Kolbe, M.; Herlach, D.M.; Shuleshova, O. Nonequilibrium solidification in undercooled Ti45Al55 melts. *J. Appl. Phys.* **2008**, *103*, 073509. [[CrossRef](#)]
14. Gao, J.; Kao, A.; Bojarevics, V.; Pericleous, K.; Galenko, P.K.; Alexandrov, D.V. Modeling of convection, temperature distribution and dendritic growth in glass-fluxed nickel melts. *J. Cryst. Growth* **2017**, *471*, 66–72. [[CrossRef](#)]
15. Draper, J.W. On the Production of Light by Heat. *Lond. Edinb. Dublin Philos. Mag. J. Sci.* **1847**, *302*, 345–359. [[CrossRef](#)]
16. Karrasch, C. Solidification Kinetics in Undercooled Pure Iron and Iron-Boron Alloys under Different Fluid Flow Conditions. Doctoral Dissertation, Ruhr University Bochum, Bochum, Germany, 2016.
17. ImageIR@8300 hs Serizes. Available online: <https://www.infratec.eu/thermography/infrared-camera/imageir-8300-hs/> (accessed on 29 September 2022).
18. Zhang, J.; Zhang, F.; Luo, X.; Zhou, Q.; Wang, H. Rapid solidification of a FeSi intermetallic compound in undercooled melts: Dendrite growth and microstructure transitions. *J. Mater. Sci.* **2019**, *55*, 4094–4112. [[CrossRef](#)]
19. Fang, Y.; Galenko, P.K.; Liu, D.; Hack, K.; Rettenmayr, M.; Lippmann, S. Thermodynamic description of metastable fcc/liquid phase equilibria and solidification kinetics in Al-Cu alloys. *Philos. Trans. R. Soc. A Math Phys. Eng. Sci.* **2022**, *380*, 20200327. [[CrossRef](#)]
20. Nagashio, K.; Nozaki, K.; Kuribayashi, K.; Katayama, Y. Dynamic process of dendrite fragmentation in solidification from undercooled Si melt using time-resolved x-ray diffraction. *Appl. Phys. Lett.* **2007**, *91*, 061916. [[CrossRef](#)]
21. Gangopadhyay, A.K.; Lee, G.W.; Kelton, K.F.; Rogers, J.R.; Goldman, A.I.; Robinson, D.S.; Rathz, T.J.; Hyers, R.W. Beamline electrostatic levitator for high energy x-ray diffraction studies of levitated solids and liquids. *Rev. Sci. Instrum.* **2005**, *76*, 073901. [[CrossRef](#)]
22. Witteveen, J.P.; van Gastel, R.; van Houselt, A.; Zandvliet, H.J.W. 3D modeling of electromagnetic levitation coils. *Curr. Appl. Phys.* **2021**, *32*, 45–49. [[CrossRef](#)]
23. Galenko, P.K.; Jou, D. Rapid solidification as non-ergodic phenomenon. *Phys. Rep.* **2019**, *818*, 1–70. [[CrossRef](#)]
24. Wert, C.; Zener, C. Interference of Growing Spherical Precipitate Particles. *J. Appl. Phys.* **1950**, *21*, 5–8. [[CrossRef](#)]
25. Raj, S.V.; Salem, J.A.; Locci, I.E.; Pawlik, R.J. Effect of directionally solidified microstructures on the room-temperature fracture-toughness properties of Ni-33(at. pct)Al-33Cr-1Mo and Ni-33(at. pct)Al-31Cr-3Mo eutectic alloys grown at different solidification rates. *Metall. Mater. Trans. A* **2002**, *33*, 597–612. [[CrossRef](#)]
26. Gangopadhyay, A.K.; Sellers, M.E.; Bracker, G.P.; Holland-Moritz, D.; Van Hoesen, D.C.; Koch, S.; Galenko, P.K.; Pauls, A.K.; Hyers, R.W.; Kelton, K.F. Demonstration of the effect of stirring on nucleation from experiments on the International Space Station using the ISS-EML facility. *NPJ Microgravity* **2021**, *7*, 31. [[CrossRef](#)] [[PubMed](#)]
27. Kurtuldu, G.; Löffler, J.F. Multistep Crystallization and Melting Pathways in the Free-Energy Landscape of a Au-Si Eutectic Alloy. *Adv. Sci. (Weinh.)* **2020**, *7*, 1903544. [[CrossRef](#)] [[PubMed](#)]
28. Barrirero, J. Eutectic Modification of Al-Si Casting Alloys. Ph.D. Thesis, Linköpings University, Linköping, Sweden, 2019.
29. Narayan Prabhu, K. Review of Microstructure Evolution in Hypereutectic Al-Si Alloys and its Effect on Wear Properties. *Trans. Indian Inst. Met.* **2013**, *67*, 1–18. [[CrossRef](#)]